Light-powered soft steam engines for self-adaptive oscillation and biomimetic swimming

Zhiwei Li[1], Nosang Vincent Myung[2, *], Yadong Yin[1, *]

[1]Department of Chemistry, University of California-Riverside, Riverside, California 92521, United States

[2]Department of Chemical and Biomolecular Engineering, University of Notre Dame, Notre Dame, IN 46556, United States

*e-mail: nmyung@nd.edu; yadong.yin@ucr.edu

Oscillation plays a vital role in the survival of living organisms in changing environments, and its relevant research has inspired many biomimetic approaches to soft autonomous robotics. However, it remains challenging to create mechanical oscillation that can work under constant energy input and actively adjust the oscillation mode. Here, a steam-driven photothermal oscillator operating under constant light irradiation has been developed to perform continuous or pulsed, damped harmonic mechanical oscillations. The key component of the oscillator comprises a hydrogel containing Fe_3O_4/Cu hybrid nanorods, which can convert light into heat and generate steam bubbles. Controllable perturbation to the thermo-mechanical equilibrium of the oscillator can thus be achieved, leading to either continuous or pulsed oscillation depending on the light intensity. Resembling the conventional heat steam engine, this environment-dictated multimodal oscillator uses steam as the working fluid, enabling the design of self-adaptive soft robots that can actively adjust their body functions and working modes in response to environmental changes. An untethered biomimetic neuston-like robot is further developed based on this soft steam engine, which can adapt its locomotion mechanics between uniform and recurrent swimming to light intensity changes and perform on-demand turning under continuous light irradiation. Fueled by water and remotely powered by light, this unique hydrogel oscillator enables easy control over the oscillation dynamics and modes, offering an effective approach to self-adaptive soft robots and solar steam engines.

Light-powered soft steam engines enable self-adaptive photothermal oscillation and biomimetic neuston-like swimming.

INTRODUCTION

Oscillation is ubiquitous at all scales in nature, from the vibration of chemical bonds (*1*) to the cytoskeletal oscillation of cells (*2*), wing oscillation of hummingbirds (*3*), and heartbeat of mammals (*4*). One notable feature of these diverse oscillations is the self-sustained periodic motion under non-periodic stimuli (*5*). In microorganisms like bacteria, oscillation determines many fundamental biological processes, properties, and functions (*6*). A noticeable example is the spatial oscillation of protein localization that defines the position of cell division and the localization of DNA (*6*). Another attractive feature of these natural oscillations is their adjustable frequency in response to environmental changes (*7*). The mammalian heartbeat oscillation is established by the sino-atrial node and has a tunable frequency of 0.83-2.5 Hz depending on surrounding blood oxygen content with constant-amplitude action potentials. These properties make biological species adaptable to ever-changing environments by actively adjusting the oscillation mechanics and body functions.

Mimicking these existing oscillating systems offers opportunities for preparing adaptive robots and energy-harvesting devices (*8, 9*). Particularly, oscillators with soft bodies are expected to realize the functions of biological species if they can perform regular oscillations under non-periodic stimuli and alter their oscillating dynamics in response to environmental changes. Artificial oscillators can be prepared using a tethered power source, such as an alternating current, to drive the periodic shape changes of materials and continuous locomotion of soft robots (*10-13*). Compared with mechanical robotic devices comprising rigid and dense materials (*14, 15*), their soft bodies can adapt to environmental changes through on-demand shape morphing (*16*). However, their mechanical work is limited by the tethered power input. Several advanced technologies use responsive materials to surrounding stimuli so that autonomous oscillation can occur (*17, 18*). A few examples include soft oscillators that are driven by heat (*19, 20*), chemical reactions (*21*), and humidity (*22, 23*). However, their further development to self-sustained soft robots is often limited by the slow responses, low oscillation frequency, and lack of remote control (*24, 25*). The sluggish heat and mass transfer inside their soft bodies is the main reason for the slow shape morphing in response to external stimuli.

Photothermal actuators utilize light as a renewable and remote energy source to power mechanical movement (*26-30*). Thanks to wireless signaling, tunable energy input, and easy directional control, light is an ideal stimulus to develop artificial soft oscillators and bionic robots. Existing strategies typically combine the phase transition of liquid crystal elastomers or hydrogels with a built-in negative feedback loop for photothermal oscillation (*31-35*). These elegant designs enabled the creation of several photothermal oscillators operating under continuous light irradiation, which, however, require stringent control of light directionality to fulfill the feedback loop requirements. Besides, their oscillation modes and

frequency are determined by the actuator mechanical properties with negligible responses to stimulus changes. Therefore, creating self-sustained, adaptive soft robots remains challenging.

Here, we develop a light-powered soft oscillator with adaptive oscillation modes in response to light irradiation of different intensities. It features a hierarchical structure, with the primary component being a photothermal actuator comprised of a polymer hydrogel and Fe_3O_4/Cu hybrid nanorods. The plasmonic property of the nanorods makes them excellent photothermal converters working at the desired wavelength. Upon light illumination, they heat up and produce steam by vaporizing the water contained in the porous hydrogels. The local steam generation leads to bubble formation, which acts as a regular perturbation to the thermo-mechanical equilibrium of the film, resembling a steam engine. The high thermal and mechanical stability allow the trilayer films to sustain long-term oscillation under continuous water supply, e.g., by partially immersing the film in water. Such flexible design is also operational for other materials, including plasmonic nanostructures with resonant absorption at a certain wavelength or "black" materials with broadband absorption for diffuse white light actuation. The potential of this soft steam engine is further demonstrated by designing a neuston-like swimming robot (NeusBot) that can move sustainably and rapidly (at a speed of ~4 body lengths per minute), with highly controllable swimming modes by modulating the light intensity.

RESULTS

Steam-driven photothermal oscillators

Hybrid Fe_3O_4/Cu nanorods are developed as photothermal converters considering the low cost and high abundance of Cu and the plasmonic activities of Cu nanorods comparable to Au counterparts (*36*). While the localized surface plasmon resonance (LSPR) of Cu nanorods allows actuating the hydrogel oscillator at a particular resonant wavelength, the broadband absorption of coupled Fe_3O_4 nanorods can also convert diffuse white light into heat to power the mechanical oscillation, making the hydrogel oscillator operational under different types of light sources. We used an unconventional confined growth to synthesize the hybrid nanorods with Fe_3O_4 nanorods (110 nm×20 nm) as templates (**fig. S1A**) (*37-39*). The seeded growth of Cu occurred in the defined gaps between Fe_3O_4 nanorods and resorcinol-formaldehyde (RF) shells (**fig. S1B**). TEM images of the hybrid structures are shown in **figs. S1C and S1D**, with one Fe_3O_4 and one Cu nanorod coupled in a parallel manner. During the seeded growth, a sharp plasmonic peak appeared at ~940 nm (**fig. S2A**), indicating the successful anisotropic growth of Cu in the gaps. The extinction spectra in **fig. S2B** reveals two plasmonic peaks, with 600 nm and 940 nm for transverse and longitudinal modes of Cu nanorods, respectively.

The configuration of the trilayer actuator is depicted in **Fig. 1A**. The middle layer is a polyacrylamide (PAM) hydrogel containing the plasmonic nanorods for converting light to heat to vaporize the surrounding water. A top polyimide (PI) layer and bottom polydimethylsiloxane (PDMS) layer are introduced to construct the trilayer actuator. With different thermal expansion coefficients, these two polymeric materials are readily available in thin films, making it straightforward to fabricate the desired structure. The great convenience in changing the geometry, shape, size of the actuators enables systematic studies of the as-designed photothermal oscillators. As discussed later, both PI and PDMS are hydrophobic, allowing the resulting films to float on the water surface to realizing Neuston-like robots. It is worth noting that the current mechanism can potentially be extended to other elastic films with different coefficients of thermal expansion, opening the door to various adaptive robots that can meet the requirements of specific applications. We first examine the hydration performance of the hydrogel layer at ambient conditions. In thermogravimetric analysis (TGA), water evaporation causes ~80% mass loss before 100 ^{o}C, with a maximum speed of 5.7%/min at 85^{o}C (**fig. S3A**). The hydrogel exhibits reliable hydration-dehydration performance, with the hydration only taking one hour to reach saturation (**fig. S3B**). Therefore, this material design enables the multiple uses of the trilayer actuators for powering different mechanical work.

The steam generation-induced photothermal oscillation is illustrated in **Fig. 1B** and **fig. S4**. Upon near-infrared (NIR) light irradiation at stage i, the film bends due to a higher coefficient of thermal expansion of PDMS than PI. As the temperature increases to its maximum value, the film reaches an equilibrium state (stage ii). With continuous light irradiation, the local high temperature vaporizes the surrounding water, producing vapor bubbles between the top PDMS and middle hydrogel layers (stage iii). The bubble serves as a gas wedge so that the trilayer actuators recover slightly to an out-of-equilibrium state. The vapor gets released when the bubble expands to the film edge, leading to a fast recovery of the actuator to its equilibrated state. The fast release of the elastic potential initiates a cycle of damped harmonic oscillation in the trilayer actuator (**fig. S4**). The continuous vapor generation and release produce constant mechanical oscillation in the actuators. To verify this hypothesis, we first used a NIR light (2.6 W/cm^2) to irradiate the film. As shown in **Fig. 1C** and **Movie 1**, the film bent at the initial 30-s irradiation, exhibiting a monotonic increase of its bending angle. This observation is consistent with the proposed stage ii. Prolonging light irradiation generated noticeable oscillation associated with fast, continuous bubble generation inside the film (**Fig. 1D** and **Movie 2**). **Fig. 1E** plots the time-resolved bending angle of the film under continuous light irradiation, which in combination with the highly correlated angular velocity, demonstrates a periodic, high-frequency oscillation along an equilibrium bending angle (**fig. S5A**). Its frequency is calculated to be 10.13 Hz by converting the bending angle signal in the time domain to the intensity signal in the frequency domain using fast Fourier transform (FFT) (**Fig. 1F**), indicating that the film oscillates ~10 times within 1s.

The photothermal oscillator has an average oscillating magnitude of 2.90°, equivalent to 0.92 mm in tip displacement (**fig. S5B**).

Tuning the frequency of the hydrogel oscillator

Thanks to the efficient photothermal conversion of hybrid nanorods, a rapid and drastic temperature rise can be induced in the hydrogel upon irradiation by the NIR light at 2.6 W/cm^2 (**figs. S6A** and **S6B).** A quasi-equilibrium state is established when the heat generation balances the heat loss due to the local steam generation and diffusion to surroundings. After 70-s irradiation, we observed a second drastic temperature increase mainly because the water in the hydrogel is exhausted, and the continued photothermal conversion boosts the temperature. Accordingly, the film bent steadily at the initial 20-s irradiation **(fig. S6C)** and then switched to continuous oscillation as indicated by the successive changes of bending angles. The oscillating magnitude decreases after 70-s irradiation, which happens right at the beginning of the second temperature rise. These observations consistently confirm the total water consumption, and the disappearance of steam bubbles causes the oscillation-to-bending transition. In addition, if the trilayer film was made with dry hydrogel, the film only bent under the same light irradiation (**fig. S6D**). Also, the films bent without noticeable oscillation if a bilayer film without hydrogel layer was used (**figs. S6E** and **S6F**). These control experiments further underpin the importance of the continuous hydration of the hydrogel layer: the absorbed water vaporizes upon photothermal heating, leading to steam bubble generation and mechanical oscillation under constant light irradiation.

Tuning the oscillation frequency is possible by simply changing the film length. **Fig. 2A** shows the oscillation of 20-mm and 35-mm films under the same light irradiation. They oscillated steadily with constant periodicity and slightly changing magnitude due to the small variation in bubble formation. The oscillation periods monotonically decreased when the film length decreased (**fig. S7A**). A close analysis by FFT indicates that the frequency increases from 10 Hz to 32 Hz with an optimal oscillation magnitude of 4° just by shortening the film from 45 mm to 15 mm (**Figs. 2B, S7B,** and **S7C**). Another important geometry parameter of the trilayer actuator is the film thickness, which is highly correlated to the stiffness of the actuators and thus determines the actuation-relaxation rate, equilibrium bending angle, and photothermal oscillation frequency. As PDMS has a much higher Young's modulus (0.75 MPa) than PAM hydrogel (~10 kPa), tuning the thickness of the bottom PDMS layer is an efficient way to recognize the critical role of actuator stiffness in determining the shape morphing and mechanical oscillation (*40, 41*). We prepared five hydrogel oscillators with the PDMS thickness increasing from 0.2 mm to 1.0 mm with a 0.2-mm step, corresponding to an increase in the total trilayer thickness from 0.4 mm to 1.2 mm. In **fig. S8A**, these trilayer

actuators first bent to approach the thermo-mechanical equilibrium under light irradiation and relaxed gradually after turning off the light, leading to thickness-dependent equilibrium bending angles. The thinnest film (0.4 mm) demonstrates the largest equilibrium bending angle of 52°, which gradually decreases as the film thickness increases to 1.2 mm (**figs. S8B and S8C**). A close analysis indicates that the equilibrium bending angle is inversely proportional to the film thickness, consistent with the analytical model in **fig. S9** (See detailed derivation of **Eqs. 1-6** in Materials and Methods section). In analyzing the bending kinetics, we plot the instantaneous angular velocity during bending and relaxation in **fig. S10**, which displays a gradual deceleration in photothermal bending and free relaxation for the five oscillators. The films experience a maximum driving force at the beginning of bending and the strongest restoring force right after turning off the light, leading to the largest angular velocities. As the bending and relaxation proceed, the film accumulates bending-induced counterforce during photothermal actuation and experiences decreasing restoring force during free relaxation, which is the main reason for such angular velocity decay. Plotting the maximum angular velocity against film thickness reveals a linear dependence in these two sequential and highly correlated processes (**Fig. 2D**). We then analyze the mechanical oscillation of these oscillators during the photothermal bending process. The mechanical oscillation of the five trilayer films is all periodic but with different oscillating characteristics under the same light irradiation (**fig. S11A** and **Movie 3**). The obvious peaks in **fig. S11B** after FFT analysis confirms the periodic mechanical oscillation and thickness-dependent oscillation frequency.

To understand the underlying physical principles and explain the dependence of photothermal oscillation on film geometry and stiffness, we introduce a theoretical oscillating model based on classical mechanics (see details in Materials and Methods section). The trilayer oscillator is considered a cantilever beam with a rectangular cross-section. According to **Eqs. 7** and **8**, the oscillating frequency of a damped harmonic oscillator decrease as the cantilever beam length (L) increases, with a decaying rate larger than $1/L^2$. In addition, the increase in film length causes more of the film surface to be exposed to light, leading to a potential increase in bubble generation and thus fast oscillation. These two competing effects cause a higher oscillation frequency in long trilayer film than predicted. To analyze the film thickness effect, we consider a cantilever beam with a rectangular cross-section, with a width of b and thickness of h. Its cross-section area (A) and the area moment of inertia (I) can be calculated by $b \times h$ and $b \times h^3/12$, respectively, and substituting these expressions to **Eq. 8** leads to the final **Eq. 9**,

which predicts a monotonic increase of oscillating frequency with the cantilever thickness. This theoretical consideration is confirmed by the upward trend in the measured frequency of films with different thicknesses (**Fig. 2E**). In addition, due to the presence of damping term in **Eq. 9**, the frequency of a damped harmonic oscillator should be lower than that of a simple harmonic oscillator (**Eq. 10**), leading to a faster

decay of oscillation frequency against thickness decrease, which is also consistent with the results in **fig. S11C,** further confirming the damped nature of the hydrogel oscillators under light irradiation.

The crosslinking ratio of the hydrogel layer also plays an essential role in controlling the oscillation frequency by determining the efficiency of steam generation. It can be achieved by adjusting the amount of crosslinker, N,N'-Methylenebisacrylamide, during photopolymerization. We prepared five hydrogels by increasing the crosslinker-to-monomer ratio from 0.014 to 0.168 (**fig. S12A**), corresponding to hydrogel polyacrylamide (h-PAM) 1 to 5. After full hydration, h-PAM1 displayed a large volume expansion (~285%) because of the low crosslinking ratio, while the volume change of h-PAM5 was small (~126%). The highly crosslinked hydrogel limits its hydration and is expected to contain less saturated water (**Fig. 3, A** and **B**). The hydration reaches saturation after 1 hour with differing maximum water contents, dropping from 1300% for h-PAM1 to 300% for h-PAM5 (**Fig. 3, C and D**). The crosslinking degree also affects the hydrogel dehydration during uniform heating. In dynamic thermogravimetry (10 ºC/min), the higher water content in h-PAM1 leads to more mass loss below 150 ºC (**fig. S12B**). In the differential thermal analysis in **fig. S12C**, the film h-PAM1 has a higher maximum mass loss rate (~11.6%/min) and lower fastest-evaporation temperature (~110 ºC) than film h-PAM5. There exist three bonding states of water in the hydrogel matrix: free water, intermediate water, and bound water (*42, 43*). The highly crosslinked hydrogel has a dense polymer scaffold and thus a large ratio of strongly bonded water under full hydration states, which may raise the evaporation enthalpy and temperature. The second peak located at a high temperature is primarily induced by the carbonization and degradation of the hydrogel under the N_2 atmosphere (*44*). The higher crosslinking degree and denser polymer matrix lead to a higher degradation temperature of the h-PAM5 film. After careful characterization, we prepared photothermal actuators using the five hydrogels as the middle layers and tracked the mechanical deformation under the same light irradiation. As shown in **fig. S13** and **Movie 4**, they exhibit variable oscillation magnitude and frequency depending on the crosslinking ratios. The frequency first increased from 6.5 Hz to 14.5 Hz and then dropped to 8.1 Hz (**Fig. 3E**). The crosslinking degree influences the ratio of water molecules in different bonding states and the mass of the actuators, which have opposite effect on oscillation. Specifically, a low crosslinking degree leads to fast water evaporation and, therefore, high-frequency oscillation. On the other hand, its high water content dramatically increases the actuator mass, making oscillation more difficult. These two competing factors produce an optimal oscillation frequency of 14.5 Hz on h-PAM4. A similar dependence was also observed on the oscillation magnitude, which has an optimal value of 8.9º for h-PAM2. The small frequency and magnitude of h-PAM1 and h-PAM5 actuators largely attribute to the large mass and slow steam generation, respectively. We observed opposite dependence between magnitude and frequency in the other three films, with high oscillation frequency for small magnitude.

Realizing long-term oscillation is possible with a continuous water supply during light irradiation. We modify our experiments by inserting one end of the trilayer film into a capillary tube containing water, which can supply the water to the middle hydrogel layer. Their mechanical oscillation at 0, 1, 2, and 3 minutes during continuous light irradiation is shown in **fig. S14A**, with a similar oscillating mode at different times. Further analysis demonstrates small changes in the oscillating frequency (~11 Hz) and average magnitude (~0.5°) among these four measurements, indicating long-term stable motion of the photothermal oscillator (**fig. S14B**). Another benefit associated with the open design of the trilayer oscillators is that they can be used multiple times by simply re-hydrating the middle hydrogel layer. By immersing the oscillator in water for one hour, the hydrogel layer absorbs maximum water, ready for next-cycle photothermal oscillation. **fig. S15A** plots the mechanical oscillation during the 1st, 6th, and 12th use of the same trilayer film, whose oscillation frequency and magnitude remain stable around 15 Hz and 2.5°, respectively, during the twelve actuating cycles (**fig. S15B**). These results demonstrate the good thermal stability of the middle hydrogel layer and the reliable mechanical stability of the trilayer films. Such oscillators can also be constructed using other photothermal converters, for example, Fe_3O_4/Ag hybrid nanorods that can leverage the high absorbance of Ag nanorods in the NIR region (*29*). Continuous mechanical oscillation could be observed when the as-fabricated trilayer film was exposed to light irradiation (**fig. S16**). This flexible material design facilitates the creation of photothermal oscillators powered by ambient white light, which is vital for the practical use of soft oscillators for energy harvesting or soft robotics. In this regard, another great benefit associated with the current design is that the mechanical oscillation is driven by steam generation and not restricted by the directionality of the incident light, making it possible to design photothermal oscillators working under diffuse light (**fig. S17A**). For example, due to the broadband absorption of Fe_3O_4, the photothermal oscillators made of hybrid Fe_3O_4/Cu nanorods still operate under a white light source (~3.0 W/cm^2), exhibiting a frequency of ~8 Hz (**fig. S17B and Movie 5**). In another experiment, we used carbon black as the photothermal converter to take advantage of its broadband absorption in the visible range (**fig. S17C**). A steady mechanical oscillation of ~10 Hz was observed under diffuse white light irradiation (**fig. S17D**).

A pulsed, damped harmonic oscillator

The light intensity is expected to have a substantial influence on the steam generation and the film oscillation. **Fig. 4A** summarizes the oscillation performance of a film under different-intensity light irradiation. Interestingly, we observe pulsed, damped harmonic oscillation powered by low-intensity light, in which the pulse frequency increases with light intensity. For example, the period between two oscillation pulses was prolonged from 0.31 s to 0.56 s, 0.83 s, and 8.33 s by decreasing light intensity from 1.4 W/cm^2

to 0.2 W/cm^2. Within each pulse, the mechanical oscillation was damped with exponential decay of its magnitude. In this characteristic oscillation mode, two oscillation periods were recognized with t_1 and t_2 for oscillation and pulse period, respectively (inset in **Fig. 4B**). Specifically, t_1 defines the duration between neighboring damped peaks, while t_2 defines the time between two successive pulses. Again, their accurate frequency can be calculated by FFT analysis. In **Fig. 4B**, two peaks exist, with f_1 in the high-frequency region for the oscillation frequency and f_2 in the low-frequency region for the pulse frequency. The former is within a range of 12.5 Hz and 15 Hz, without apparent dependence on light intensity (**Fig. 4C**), while the latter increased from 0.12 Hz to 1.20 Hz, 1.80 Hz, and finally 3.19 Hz with light intensity (**fig. S18**). The low light intensity induces a small temperature increase in the hydrogel layers and leads to slow steam generation and periodic bubble formation. As the steam bubble reaches the film edge, the high pressure releases the vapor to the surroundings, initiating one-pulse oscillation. In a close investigation, we carefully monitored the steam bubble generation during light irradiation and simultaneously tracked the film vibration. The digital photos in **Fig. 4, D** and **E** show the bubble size changes and the corresponding tip displacement of the actuators. The bubble expands to a critical size, releases the vapor from the film edge (stage i to stage ii in **Fig. 4D**), and then gradually decreases to minimal size (stage ii to stage v). During stages i and ii, the film unbends slightly and then oscillates around the bending equilibrium (**Fig. 4E**). **Fig. 4, F** and **G** shows a step-by-step correlation between bubble generation and film oscillation. Each bubble generation triggers one pulse of the mechanical oscillation. The wedging effect of the vapor bubble is evidenced by the initial slight unbending of the film (stage i to stage iii). Notably, the mechanical response lagged slightly behind the bubble size changes. The film keeps unbending from stage ii to stage iii when the bubble size decreases, largely because the bent film needs a short time to reach another mechanical equilibrium when bubble size decreases.

Biomimetic self-adaptive soft swimmer

The light-powered oscillation offers many opportunities in designing various smart materials and devices. In this work, we demonstrate a biomimetic design of a self-adaptive soft photothermal swimmer that can mimic neuston to move and turn freely on water surfaces. Neuston is a collective set of living organisms that can swim on or just below the water surface (*45*). The most known are water striders that rely on water surface tension or buoyancy to swim (*46, 47*). Their water-repelling legs act as paddles to enable quick movement on the water surface. One attractive feature is their propulsive motion, which relies on discontinuous paddling to drive pulsed movement. To mimic this unique swimming behavior, one needs to accurately modulate the actuating mode of the soft robots so that continuous energy input can produce both successive and pulsed movement on the water surface. Since the outside PI and PDMS layers are

hydrophobic, the trilayer actuator can float on the water surface. For supporting smooth locomotion, a continuous water supply is required to compensate for water consumption by local steam generation. Therefore, we designed a dome-shaped actuator by stretching the initial elastic PDMS layer by ~20% during fabrication (**fig. S19**), which produced a 120° curvature (**Fig. 5A**) (*48*). As revealed in **Fig. 5B**, the two ends of the curved actuator have close contact with water, through which water can be efficiently transported to the middle hydrogel matrix. Irradiating one end of the curved actuator leads to the photothermal oscillation at this end, which in turn propels the swimmer forward (**Fig. 5C**). A soft neuston-inspired robot (Neusbot) can be powered by continuous light irradiation with adaptive swimming modes and superior swimming performances. To demonstrate the photothermal oscillation underwater, we first designed a simple experiment by immersing one film end in water. As shown in **fig. S20** and **Movie 6**, we observed pulsed water wave propagation generated by film oscillation under continuous 980-nm laser irradiation, confirming the mechanical oscillation of the submerged actuators upon laser irradiation.

We started with a 2-mm long curved film and observed its locomotion at the water-air interface using a 980-nm laser with a beam diameter of 3.8 mm. As summarized in **Figs. 5D and S21**, continuously irradiating one end propels the film to swim toward the other end along a near-linear path. The swimming speed increases obviously with light intensity. The swimming process was tracked using modeling software to evaluate the Neusbot's swimming performance accurately. We first measured relative Neusbot displacement in real-time for Neusbot powered by lasers of different intensities (**Fig. 5D**), revealing laser intensity-dependent locomotion with a monotonic increase in path lengths (**Movie 7**). Interestingly, a close analysis of the path curve indicates that it is non-uniform for Neusbot powered by low-intensity laser (from 0.2 W to 0.8 W with a beam diameter of 3.8 mm) but near-uniform under 1.2-W laser irradiation with the same bean diameter. The non-uniform motion is progressive and periodic (**Movie 8**). The real-time Neusbot positions propelled by different power inputs are further mapped in **Fig. 5E**, confirming their linearly forward movement at the water-air interface by the small displacement in the y-axis. On the other hand, 1.2-W laser irradiation leads to uniform position changes along the x-axis, which is consistent with a linear dependence of path length on irradiation duration. For other power inputs, the x-axis displacement has successive, periodic changes with the same time intervals. The insets in **Fig. 5E** highlight one-period displacement changes for films powered by low-intensity lasers (from 0.2 W to 0.8 W with a beam diameter of 3.8 mm). Considering the same time intervals between neighboring positions, a small step size implies slow swimming at both the beginning and end of each cycle. The large step size in the middle of each cycle demonstrates the fast swimming under continuous laser irradiation. These observations collectively suggest that the Neusbot swims with apparent acceleration-deceleration cycles under low power inputs. The period for the acceleration-deceleration cycle increased from 2.168 s to 2.335 s, 2.502 s, and finally, 3.335 s when the laser intensity decreased from 0.8 W to 0.2 W with a beam diameter of 3.8 mm. The corresponding

displacements during the swimming cycle are 2.25 mm, 1.73 mm, 1.54 mm, and 0.79 mm. The presence of the periodic swimming mode at low energy inputs and its transition to a continuous, uniform swimming mode results from the self-adaptive mechanical oscillation in response to light intensity changes. The pulsed mechanical oscillation under low energy inputs induces well-separated swimming cycles. Between two successive pulses is the film equilibrium state, leading to apparent stops between swimming cycles under continuous light irradiation. Increasing light intensity induces continuous mechanical oscillation, which is expected to propel a uniform, consistent swimming.

The swimming mechanism is further verified by monitoring the real-time velocity changes during laser-powered Neusbot swimming. As shown in **Fig. 5F**, we observed periodic changes in the swimming velocity at low energy inputs, featuring first acceleration and then deceleration in one cycle. The frequency of velocity change increases from 0.332 Hz to 0.465 Hz as the input power is raised to 0.8 W with a beam diameter of 3.8 mm (**fig. S22**), which is consistent with the path length analysis. The Neusbot powered by the high-intensity light (1.2 W, 3.8-mm beam diameter) swims at a roughly constant velocity as its real-time velocity only fluctuates without noticeable regular changes (**Movie 8**). The average velocity reaches ~1.3 $mm*s^{-1}$ at 1.2 W with an equivalent velocity of ~4 body length (BL)$*min^{-1}$ (**fig. S23A)**. The linear dependence of average velocity on laser intensity suggests that it is possible to further enhance the swimming performance by simply increasing laser intensity. The peak velocity is also found to monotonically increase with light intensity. In addition, the swimming performance is stable for an extended period. For example, the Neusbot can swim forward steadily for ~45 s, during which we did not observe apparent speed drop or changes in its swimming manner (**figs. S23B-C**). The good performance of this artificial Neusbot is highlighted by comparing its relative swimming velocity against body weight with that of living animals (dots), both nekton and neuston, and reported soft swimmers (circles), as presented in **Fig. 5G**. Notably, the relative swimming velocity is introduced in BL per minute, which is more ecologically relevant than the absolute velocity and broadly used for performance assessment (*10, 49*). For chordate nekton, their relative swimming velocity decreases as body weight increases (*50, 51*), primarily because of similar scaling of mechanical constraints on their swimming performance occurring on mammals (*49*). Neustons, like water striders or water spiders, can move up to 10^4 BL per minute due to low resistance on the water surface and their light bodies (*52*). The biomimetic Neusbot has a high swimming velocity than previously reported soft swimmers while featuring comparable body weight. At current power inputs, the Neusbot performance is approaching the bottom limit of living neuston and nekton.

To further understand the mechanism of the fast-swimming behavior, we performed similar measurements using a bilayer actuator as a control experiment. The structural details of the bilayer and trilayer actuators and the differences between them are illustrated in **fig. S24A**. Particularly, the middle hydrogel layer was

removed, and Fe_3O_4/Cu nanorods were incorporated in the PDMS layer for photothermal conversion. Under both periodic (0.4 W, 3.8-mm beam diameter) and continuous (1.2 W, 3.8-mm beam diameter) swimming modes, the velocity is much higher for the trilayer actuator than the bilayer one (**fig. S24B** and **Movie 9**). Within 20-s observations, the path length of the NeusBot is ~20 fold higher (**fig. S24C**).

Turning the Neusbot toward the desired direction by laser irradiation is another important feature for achieving biomimetic functions. **Fig. 6A** (i) illustrates the operation for clockwise rotation by irradiating the left side of the Neusbot's head using a 980-nm laser with a diameter of 3.8 mm (0.8 W). Tracking the real-time positions of the film end and head indicates a smooth rotation with tacked laser irradiation in **Fig. 6A** (ii). Similarly, irradiating the right side of the film head, as illustrated in **Fig. 6B** (i), leads to counterclockwise rotation in **Fig. 6B** (ii). The real-time film positions demonstrate a pure rotation with negligible translational displacements in the two rotations (**Movie 10**). In clockwise rotation, the x-coordinate is $\pi/4$-phase ahead of y-coordinate (**Fig. 6C**), while counterclockwise, the y-coordinate is ahead with the same phase difference (**Fig. 6D**). Under a particular power input, the Neusbot has a constant angular velocity ($23.3^{o}\cdot s^{-1}$), leading to a linear increase of its rotation angle (**Fig. 6E**). The polar plot in **Fig. 6F** further confirms that the Neusbot can turn to any desired direction by controlling the duration of laser irradiation.

DISCUSSION

A photothermal oscillator has been developed by integrating the plasmonic photothermal steam generation with the mechanical perturbation associated with the formation and collapse of steam bubbles. The local steam bubble generation inside the trilayer film acts as a steam engine and induces controllable and regular perturbation to the thermo-mechanical equilibrium of the actuators. This working mechanism enables convenient control over the oscillating modes and mechanics, leading to damped, pulsed harmonic oscillation under low light intensity. Inspired by the free movement of living neustons on the water surface, we have further developed a biomimetic approach to designing a soft swimmer by taking advantage of the unique mechanical oscillation of the actuators under continuous light irradiation. This Neusbot has demonstrated adaptive continuous or periodic swimming modes in response to input powers on the water surface. It can swim at a high velocity for a considerable long time due to the high-frequency oscillation and the successive water transportation in the hydrogel matrix for powering continuous steam generation.

This photothermal oscillator uses steam as the working fluids, resembling the classic steam engine. The working mechanism presents a reliable approach to design soft actuators to power mechanical oscillation under continuous light irradiation. Relying on the high water content of middle hydrogel layers, the oscillator can work under both air and water, making it highly operational for powering mechanical

oscillation in different working conditions. However, due to the small volume of the hydrogel layer, the current design can only sustain short-term oscillation, limiting its use in practical applications. One reliable way to overcome such a limitation is to introduce a continuous water supply for long-term oscillation or re-hydrate the hydrogel layer for multiple uses of the trilayer oscillators. The oscillation frequency can be tuned over a broad range by controlling film geometry, dimension, and light intensity. Analytical models are also provided to help understand the correlation between oscillation and bending performance with the physical properties of the oscillators. These theoretical considerations provide a qualitative description of the oscillator performance, making it possible to design soft robotics with desirable performances and features. At the current stage, it is difficult to precisely predict the oscillation frequency of the trilayer oscillators due to the trilayer structure and the unique working mechanism. Further extensive studies are still required to derive an analytical solution, which can provide an integrated model to treat the physical properties of the trilayer films properly and to combine the evaporation kinetics in the hydrogel layer with the oscillation mechanics of the films.

In practice, this working mechanism is feasible to other material systems by simply changing the photothermal converters or the active PDMS and passive PI layers, therefore releasing the design of hydrogel oscillators from the restriction by specific materials. Specifically, the hydrogel oscillators can work under both focused laser and diffuse white light if a proper photothermal converter is used, including plasmonic particles with resonant absorbance at a specific wavelength and “black” materials with broadband absorption across the visible spectrum. Another advantage associated with the working mechanism is the multimodal and self-adaptive oscillation in response to light intensity changes, enabling the design of biomimetic robotics with many unique actuation manners, such as the pulsed swimming mode of the Neusbot. There are several advantages to introducing multimodal mechanical oscillation and biomimetic swimming. It allows the development of biomimetic robotics that can mimic the unique motions of living species, like the pulsed motion of water striders. Besides, the pulsed oscillation and swimming offer higher instantaneous bending and swimming velocity than a regular, continuous swimming mode, which may provide higher mechanical energy in developing solar steam engines. More importantly, introducing multimodal oscillation may increase the degree of freedom to control the motion of soft robotics, allowing the creation of smart and multifunctional robots. Therefore, the open design allows applying the unique oscillating mechanism to many materials to develop self-sustained, adaptive soft robotics. The continuous oscillation under constant ambient conditions and its ability to adjust the oscillation dynamics in response to changing environments provide many opportunities to design self-sustained, adaptive bionic robots for potential applications in water treatment, disinfection, and waterway transportation.

Materials and Methods

Chemicals and materials

Polyacrylic acid (PAA, MW=1800), iron chloride hexahydrate ($FeCl_3 \cdot 6H_2O$), tetraethyl orthosilicate ($C_8H_{20}O_4Si$, TEOS), 3-aminopropyl-triethoxysilane ($C_9H_{23}NO_3Si$, APTES), polyvinylpyrrolidone (PVP, MW=10000), Tetrakis(hydroxymethyl)phosphonium chloride (THPC), resorcinol, formaldehyde, 2-Hydroxy-2-methylpropiophenone (used as a photoinitiator in polymerization) and hydrazine hydrate (reagent grade, 50-60%) were purchased from Sigma-Aldrich. Ammonium hydroxide ($NH_3 \cdot H_2O$) was purchased from Fisher Scientific. Diethylene glycol (DEG) was from Acros Organics. The monomer, acrylamide (AM), and the crosslinker, N,N'-Methylenebisacrylamide (BIS), were purchased from Fluka. Ethanol was purchased from Decon Labs. SYLGARD 184 silicone elastomer curing agent and SYLGARD 184 silicone elastomer base were bought from Dow Silicones Corporation. All chemicals are used directly without further purification.

Synthesis of FeOOH nanorods

10.8 g of $FeCl_3 \cdot 6H_2O$ was dissolved in 400-mL deionized (DI) water. The solution was heated to 87 ^oC for 18 hours. The supernatant was discarded, and the FeOOH nanorod precipitates were washed by deionized water three times at 11000 revolutions per minute (rpm) for 15 minutes. The final product was dispersed in 40-mL DI water.

Silica coating and polyol reduction

FeOOH was first modified by PAA. 216 mg of PAA was dissolved in 600-mL DI water, and 10 mL of the above FeOOH aqueous dispersion was added. The surface modification was carried out overnight. FeOOH nanorods were recovered by centrifugation and washed with DI water three times (11000 rpm for 15 minutes each time). The FeOOH-PAA nanorods were dispersed in 12-mL DI water. For silica coating, 4 mL of FeOOH dispersion was concentrated into 2 mL and added to 40 ml of ethanol followed by 250-μL ammonium solution (28%). 200-μL TEOS was used, which produced 5-nm SiO_2 coating. FeOOH@SiO_2 nanorods were separated from the reaction solution by centrifugation at 14500 rpm for 10 minutes and then washed with ethanol once and water three times. FeOOH@SiO_2 nanorods were reduced to magnetic nanorods in DEG at 220 ^oC. In a typical process, 15 mL of DEG was heated to 220 ^oC under nitrogen flow, and 250-μL FeOOH@SiO_2 aqueous solution was injected in the hot DEG solution. The reduction was kept for ~5 hours under nitrogen protection. The final Fe_3O_4@SiO_2 nanorods were washed by ethanol and water three times and dispersed in 12 mL of ethanol for the following surface modification.

APTES modification

The dispersion of magnetic nanorods in ethanol was added into 50-mL ethanol. Then it was heated to 78 ^oC, and 200 μL of APTES was added. The surface modification usually took 5 hours under nitrogen protection. The as-prepared product was washed with ethanol several times and dispersed in 12 mL of ethanol.

Au seeds preparation and attachment

In a typical procedure, 12 μL of THPC and 250 μL NaOH (2M) were added to 45 mL of Milli-Q water. After 5 minutes, 2-mL $HAuCl_4$ (1%) was added. The solution was covered with foil and stirred overnight. Afterward, it was stored at 4^oC as a stock seed solution. 3-mL magnetic nanorods in ethanol were centrifugated and washed with DI water twice. It was dispersed in 5-mL DI water and added into 20 mL of Au seeds stock solution. The mixture was stirred for about 1 hour. Au seeds were attached to the surface of magnetic nanorods through electrostatic interaction.

Excess Au seeds were discarded after centrifugation at 14500 rpm for 10 min. Afterward, 5 mL of DI water was added to disperse the solid rods.

PVP modification

The above dispersion was transferred to 10 mL of PVP solution (20 mg/mL, MW=10000) under sonication. The mixture was stirred overnight at room temperature, and excess PVP was removed by centrifuge at 14500 rpm for 10 minutes. The nanorods were washed by DI water twice and dispersed in 28 mL of DI water.

RF coating

13 mg of resorcinol and 18 μL of formaldehyde were added into that dispersion sequentially. After that, the mixture was heated to 50 °C, and 100-μL ammonium solution (2.8%) was added. The reaction was kept at 50 °C for 2 hours and heated to 100 °C. The reaction temperature was raised to 100 °C for the condensation of RF polymers. Meanwhile, the SiO_2 shell was etched, forming a gap between magnetic nanorods and RF nanoshells with Au seeds inside due to the alkaline condition. 5 hours later, the final products were washed with Milli-Q water three times and dispersed in 2 mL of Milli-Q water.

Confined growth of Cu nanorods

The seeded growth of Cu nanorods was performed in aqueous solutions. In a 2-mL Milli-Q water, 200-μL PAA (18 mg/mL), 120-μL Hydrazine hydrate, 20-μL $CuCl_2$ (0.2 M), 50 μL of the above seed solution was added in sequence. The reaction solution was placed in a 60 °C water bath for 30 minutes. The hybrid Fe_3O_4/Cu@RF nanorods were washed by water three times and dispersed in water.

Preparation of PDMS and PAM films

In a typical process, silicone elastomer curing agent and silicone elastomer base were thoroughly mixed with a mass ratio of 1:10. The mixture was cured at 60 °C for 2 hours to form highly crosslinked PDMS films. Hydrogel PAM (h-PAM) films were prepared by photoinitiated polymerization. In preparing the curing solution, the hybrid nanorods were dispersed in the precursor solution of PAM, containing ethylene glycol (1 mL) as the solvent, acrylamide (250 mg) as the precursor, 2-Hydroxy-2-methylpropiophenone (6 μL) as the photoinitiator, and BIS as the crosslinking agent. After fully dispersing the rods in the solution, the mixture was carefully added into the empty spaces between the PDMS and PI layers (see the next section for a detailed description). UV light was irradiated from the transparent PDMS side for ~2 minutes to cure the polymer. To prepare hydrogel with different crosslinking ratios, 3.5 mg, 7 mg, 14 mg, 28 mg, and 42 mg of BIS were added for h-PAM1, h-PAM2, h-PAM3, h-PAM4, and h-PAM5, respectively.

Fabrication of photothermal oscillators

The working mechanism of the photothermal actuators is based on different thermal expansion of polymers. A PDMS layer and a PI layer are used as the active layer and passive layer, respectively. As the PDMS layer has a high coefficient of thermal expansion (100×10^{-6} K^{-1}) than that of the PI layer (20×10^{-6} K^{-1}), the PDMS layer bends more than the PI layer does. Because the working mechanism proposed in this work needs continuous steam generation to induce perturbation to the thermo-mechanical equilibrium of the bent film, we introduced a hydrogel layer to serve as a middle layer. To this end, polyacrylamide (PAM) was used. The reasons for choosing PAM for the hydrogen layers include several aspects. Firstly, PAM is a hydrophilic polymer that can hold plenty of water molecules depending on its crosslinking ratio. Secondly, its hydrophilicity is compatible with the hydrophilic hybrid nanorods so that the

nanorods can be dispersed well in the polymer matrix. Thirdly, the crosslinking ratio of PAM can be readily tuned by changing the amount of crosslinker during polymerization. Lastly, its polymerization can be initiated by light irradiation, which facilitates robot fabrication.

During fabrication, a PDMS template was attached to a commercial PI tape with the same shape. The thickness of the hydrogel layer is primarily determined by the PDMS template. In our current design, the hydrogel thickness is ~100 μm. The width and length of one separated hydrogel layer are 7 mm and 10 mm, respectively. PDMS can strongly bind to PI tape, and periodic gaps create empty spaces between the PDMS and PI layers. The hydrogel precursor solutions were then infilled into the gaps between the top PDMS and the bottom PI layers. Since PDMS is transparent, the PDMS layer is on the top during fabrication so that UV light can penetrate through this top PDMS layer and initiate the radical polymerization of the middle PAM layer. Polymerization was performed *in situ* by irradiating the film using UV light with a wavelength of 254 nm for 3 minutes. After fabrication, the resulting trilayer was flipped over, leaving the PI as the top layer and PDMS as the bottom layer. The photothermal actuators are intentionally designed into such a shape for three reasons. First, the use of PDMS templates is to ensure the photothermal bending of the trilayer. The joints between two adjacent PAM hydrogel pieces can strongly bind to the top PI layer. The photothermal expansion of the bottom PDMS layer induces upward bending upon laser irradiation, leading to the indispensable thermo-mechanical equilibrium in the film. Second, the separated hydrogel pieces act as heating compartments, which confine the nucleation of air bubbles and make the shape morphing and mechanical oscillation controllable. Third, the escape of vapor bubbles also benefits from the two-side open structure, limiting the bubble movement along the longitudinal direction of the film, allowing the easy release of the vapor from the two sides, and leading to fast and regular mechanical oscillations upon continuous light irradiation.

In performing photothermal actuation, one end of the trilayer was fixed to a clip, and NIR light was shined on the trilayer film. Under NIR light irradiation, the trilayer actuator first bent upward toward the top PI layer due to the high thermal expansion of the bottom PDMS layer. Under continuous light irradiation, the water molecules in the hydrogel matrix vaporize so that steam forms between the top PDMS and bottom PI layers. The steam bubbles appear at the middle layer, serving as air wedge and inducing unbending the trilayer film to another equilibrium state. As the bubble size maximizes, the vapor releases from the film edge, leading to a quick drop in the bubble volume. The disappearance of the air bubble is so fast that the elastic potential in the trilayer film is converted to mechanical oscillation. It is possible to control the oscillation mode by simply changing the light intensity. In experiments, a NIR light bulb was used to power the mechanical oscillation of the trilayer film. In the case of continuous mechanical oscillation presented in **Figs. 1** to **3**, the NIR light bulb is used with a light intensity of 2.6 W/cm^2.

Fabrication of biomimetic swimmers

The three-layer actuator was designed in a dome shape to facilitate water transport in the middle hydrogel layer. To this end, the bottom PDMS layer was stretched before being attached to the hydrogel and PI layer (**Fig. S10**). The film was exposed to UV light through the PDMS side, and the middle hydrogel layer was polymerized. After UV curing, the bottom PDMS layer was relaxed to its initial state, leading to the bending of the three-layer structures. Since the PDMS layer was on the bottom, its relaxation to the initial length would lead to a dome shape (digital pictures shown in **Fig. 4A**). Notably, the PI and PDMS are the top and bottom layers in such a configuration, respectively. Our results

indicated that stretching the PDMS payer by 120% induced 120° bending in the trilayer structures. The dome-shaped actuator can stay steadily at the air-water interfaces because the bottom PDMS layer is hydrophobic. Its two ends have large contact with bottom bulk water so that water molecules can efficiently migrate to the middle hydrogel layers. A 980-nm laser was used to irradiate the biomimetic swimmers.

Characterizations

Regular TEM images were taken on Tecnai 12 transmission electron microscope operating at 120 kV. The extinction spectra were measured by the Ocean Optics HR2000 CG-UV-NIR high-resolution spectrometer. The aqueous dispersions of nanoparticles were used for the measurements. Optical microscopic images were acquired by a ZEISS microscope. The temperature changes were measured using a thermal imaging camera, and the bending angles of the trilayer films were recorded using a digital camera. A digital camera with 240 frames per second (fps) was used to track the high-frequency oscillation, and the real-time bending angles were analyzed in each frame. TGA was performed on EXSTAR series thermal analyzers.

Statistics

Error bars represent the standard deviation (SD) of three measurements in experiments. During the experiments, three measurements were performed, and the results were averaged to get the mean values and SD of each measurement. In Figs. 2C, 3E, S7B, S7C, and S23A, the SD was calculated based on three cycles of mechanical oscillation of one sample. After the middle hydrogel was hydrated, the trilayer film was exposed to light, and its oscillation frequency was carefully measured during photothermal actuation. After that, the film was immersed in water again for the second-round oscillation. This process was repeated three times, and the obtained results were averaged to get the mean values and SD. In characterizing the hydration performance of PAM hydrogels, hydrogels of a particular crosslinking ratio were prepared independently three times, and their mass during hydration and dehydration was measured. The mean values and SD were calculated using the same method and plotted in Figs. 3C and 3D.

Theoretical bending models of the photothermal oscillators

Theoretical models are developed based on the film's mechanical properties to understand the dependence of mechanical shape morphing and oscillation on the geometry of the trilayer film. We first consider a thermal expansion model to explain the photothermal bending of the trilayer film under light irradiation. According to the definition of the coefficient of thermal expansion (α_V), the volume expansion of an elastomer is determined by the temperature:

$$\alpha_V = \frac{1}{V}\left(\frac{\partial \mathrm{V}}{\partial \mathrm{T}}\right)_P \quad (1)$$

where V is the volume of the elastomer, and such thermal expansion happens under constant pressure (P). This equation describes how the size of a soft elastomer changes with a change in temperature in terms of volume fractional change per degree change in temperature at a constant pressure. A solid with a large coefficient of thermal expansion is expected to have a large volume expansion upon temperature increases. In our design, the top polyimide layer and bottom PDMS layer of the trilayer film have a coefficient of thermal expansion of 20×10^{-6} K^{-1} and 100×10^{-6} K^{-1}, respectively. The much higher coefficient of thermal expansion of the PDMS layer than that of the PI layer explains the upward bending of the trilayer during light irradiation.

On the other hand, it allows us to calculate the volume expansion of a soft elastomer against temperature changes:

$$\Delta V = \alpha_V V \Delta T \quad (2)$$

which indicates a linear dependence of volume changes in response to temperature changes for a solid with a constant coefficient of thermal expansion. If the α_V is a function of temperature, the equation to calculate the volume changes is as follows:

$$\Delta V = V \exp\left(\int_{T_i}^{T_f} \alpha_V(T)\, dT\right) - V \tag{3}$$

which also suggests volume expansion for solids with a positive coefficient of thermal expansion upon temperature increases. In addition, this equation also implies that the volume change rate (ΔV/V) is the same for films with different thicknesses if their temperature changes (ΔT) are identical upon light irradiation.

We derive an analytical solution for the coorelation between the film thickness (h) and the bending angle (α) based on these theoretical considerations. We consider five films with the same length (*L*), width (*b*) but different thicknesses (**fig. S8A**). Based on the definition of stiffness ($k=F/\delta$, where F and δ are the force and displacement on the film), a thicker film has higher stiffness, thus leading to a smaller bending angle, which is qualitatively consistent with the experimental results in **figs. S8A** and **S8B**. Since the middle hydrogel and the concentration of Fe_3O_4/Cu nanorods are the same for these five samples, it is reasonable to assume that the final temperature (T_f) and temperature changes (ΔT) in the five samples are the same under identical light irradiation. Based on **Eq. 2**, their volume expansion ratio (ΔV/V) should be equal at the equilibrium bending position. In calculating the ΔV, the volume expansion along the length is considered to estimate the overall volume changes due to the negligible changes along the film thickness and width. In **fig. S9**, the inner diameter (r) for the bent film can be calculated by r=L/α. Therefore the area for the dashed area is

$$\frac{\alpha}{2}(r+h)^2 - \frac{\alpha}{2}r^2 = \frac{\alpha h}{2}\left(2\frac{L}{\alpha} + h\right) \tag{4}$$

The final volume (V_f) of the bent film can be estimated by

$$V_f = \frac{\alpha h}{2}\left(2\frac{L}{\alpha} + h\right) b = hLb + \frac{1}{2}\alpha h^2 b \tag{5}$$

And the volume change ratio (ΔV/V) can thus be estimated by the following equation:

$$\frac{\Delta V}{V} = \frac{V_f - V}{V} = \frac{hLb + \frac{1}{2}\alpha h^2 b - hLb}{hLb} = \frac{\alpha h}{2L} \tag{6}$$

Since the volume change rate (ΔV/V) is the same for the five samples, the equilibrium bending angle is inversely proportional to the film thickness. To confirm this dependence, we performed reciprocal fitting of the scatters in **fig. S8B**, with $y=1/(a_1+a_2x)$, where a_1 and a_2 are constant. This fitting curve is presented in the red lot in **fig. S8B**, with $R^2=0.96$. The value of a_1 and a_2 based on the fitting curve is 0.0047 and 0.035, respectively. The considerably small value of a_1 theoretically confirms the reasonable accuracy of our analytical model and further points out that the equilibrium bending angle is inversely proportional to the film thickness.

Theoretical oscillation models of the photothermal oscillators

We then consider a model for understanding the mechanical oscillation of the trilayer film under light irradiation. In classical mechanics, the Hooke's law states that the force (F) of a simple harmonic oscillator (such as cantilever beam or spring oscillators) is proportional to the displacement (x): $F=-kx$, where k is positive constant. In elastic polymers, k is defined as stiffness with an expression of F/x to quantitatively describe their elastic deformation and measure polymer mechanical properties under external stresses. The angular frequency (ω_0) of the simple harmonic oscillator can be described as $\omega_0=(k/m)^{0.5}$, where m is the mass of the oscillator. In principle, the ideal simple harmonic oscillator vibrates along an equilibrium position with constant magnitude and frequency. In practice, however, due to friction,

shearing strain, and universal conversion of mechanical energy to thermal energy during practical oscillation, the mechanical oscillation is commonly damped, with gradually decreasing magnitude. To further describe the mechanical oscillation of damped harmonic oscillators, a damping ratio (ζ) is introduced to describe the oscillator frequency with a formula of $0.5c(mk)^{-1}$, where c is the damping coefficient. Therefore, the oscillating frequency (ω_1) of a damped harmonic oscillator is given by $\omega_0(1-\zeta^2)^{0.5}$. In classic mechanical oscillation, there are three types of damped harmonic oscillations depending on the value of ζ, which are overdamped ($\zeta>1$), critically damped ($\zeta=1$), and underdamped ($\zeta<1$) oscillators. In the first two cases, the large damping ratio causes the oscillator to relax to the steady-state without oscillation. In the underdamped case, the oscillator relaxes to the steady-state through continuous mechanical oscillation with oscillating magnitude gradually decreasing to zero.

To describe the mechanical oscillation of the trilayer film under light irradiation, we consider a cantilever beam model since one end of the trilayer film is clipped and the other is relaxed during our experiments. According to the literature, the angular frequency of a damped harmonic cantilever beam is highly related to the beam geometry and can be calculated by the following equation.

$$\omega_1 = \omega_0\sqrt{1-\frac{c_0^2L^4}{4\rho AEI}} \tag{7}$$

The ω_0 is the angular frequency of the first bending mode without damping and can be approximated by $3.5(EI/\rho AL^4)^{0.5}$. In these expressions, c_0, L, ρ, A, E, I are damping coefficient per unit cantilever length, cantilever length, cantilever density, the cross-sectional area of the cantilever, Young's modulus, and the area moment of inertia, respectively. Substituting the expression of ω_0 into **Eq. 7** leads to the following formula for calculating the damped oscillation frequency.

$$\omega_1 = 3.5\sqrt{\frac{EI}{\rho AL^4}}\sqrt{1-\frac{c_0^2L^4}{4\rho AEI}} = 3.5\sqrt{\frac{EI}{\rho AL^4}-\frac{c_0^2}{4\rho^2A^2}} \tag{8}$$

The oscillating frequency (f_1) can be calculated by $\omega_1/2\pi$. Considering the results in **Fig. 3A**, it is reasonable to assume that the mechanical oscillation of the trilayer film is underdamped because it relaxes to an equilibrium state through continuous oscillation with a gradually decreasing magnitude. A few forces or factors that may damp the mechanical oscillation include air resistance during oscillation, the non-elastic deformation in each polymer layer at high temperature, and the possible shearing force, plastic deformation, and displacement at the two interfaces of the trilayer film. Particularly, the trilayer is joined together by the PDMS templates. The hydrophilic middle PAM layer is not sticky with the hydrophobic top PI layer and bottom PDMS player, leading to loose interfaces between these layers. Therefore, shearing forces and considerable displacement may exist between the two neighboring layers, significantly depleting the elastic potential energy and thus damping the mechanical oscillation. These facts indicate that mechanical oscillation of the trilayer films is highly damped and requires continuous steam generation for powering a continuous mechanical oscillation. Despite the multiple layers of the film and the complex interfaces between each layer, it is still possible to qualitatively interpret the dependence of the oscillation mechanics on the film geometry based on the classic harmonic oscillation theory.

We first analyze the effect of film length on the oscillating frequency. Previous considerations predict that the oscillation frequency of a simple harmonic oscillator is inversely proportional to the length square of the oscillator. However, in **Fig. 2C**, we observe a slower decay of oscillating frequency when the film length increases from 15 mm

to 45 mm than predicted by the harmonic oscillation model. According to **Eq. 8**, the oscillation frequency (ω_1) of a damped harmonic oscillation is calculated by scaling the frequency of the corresponding harmonic oscillation to a damping term, $(1\text{-}c_0^2L^4/4\rho AEI)^{0.5}$, which has a positive value between 0 and 1 and thus predicts an even lower frequency compared with that of a harmonic oscillation. On the other hand, the area heated by the light source increases as with the length, leading to fast steam bubble generation and thus an increase in the magnitude of the driving force. This sequence of events increases the frequency of the mechanical oscillation. Therefore, increasing film length has two opposite effects, resulting in an overall slower decay of the oscillating frequency against cantilever length than the predicted frequency of a damped harmonic oscillator.

The dependence of oscillation frequency on film thickness is plotted in **Fig. 2E**, showing a gradual increase in film thickness. Specifically, the frequency increases from ~5.8 Hz to ~17.0 Hz when the film thickness increase from 0.4 mm to 1.2 mm. To theoretically analyze such dependence, we start with **Eq. 8** and substitute cross-sectional area (A) and the area moment of inertia (I) into this equation. Since the film has a rectangular cross-section with a thickness of *h* and width of *b* and the bending and oscillation occur along the b-axis, its area moment of inertia and cross-sectional area can be calculated by $bh^3/12$ and bh, respectively. Therefore, the frequency of the damped hydrogel oscillator can be calculated by the following equation.

$$\omega_1 = \frac{3.5h}{L^2}\sqrt{\frac{E}{12\rho}}\sqrt{1-\frac{3c_0^2L^4}{\rho Eb^2h^4}} \tag{9}$$

The ω_1, c_0, ρ, and E are oscillation frequency, damping coefficient per unit cantilever length, cantilever density, and Young's modulus, respectively. This equation predicts that decreases in film thickness lead to a simultaneous decrease in oscillation frequency. For a harmonic oscillator without damping, its frequency can be simply predicted by the following equation.

$$\omega_0 = \frac{3.5h}{L^2}\sqrt{\frac{E}{12\rho}} \tag{10}$$

Also, due to the presence of a damping term (with a value between 0 and 1) in **Eq. 9**, the decreasing rate of the oscillation frequency should be larger than that of the film thickness. We use the 1.2-mm film as a reference, and the decay of oscillation frequency of a harmonic oscillator against film length is predicted by **Eq. 10** and is represented by the dashed black curve in **fig. S10C**. In our measurements, the observed oscillation frequency is lower than the predicted frequency of a harmonic oscillator based on **Eq. 10**, and the frequency decay of the trilayer film against film thickness is faster than that of a harmonic oscillator, both of which demonstrates good agreement of the measurements with the damped harmonic oscillation model.

Supplementary Materials and Methods

References

1. G. Busca, J. Lamotte, J. C. Lavalley, V. Lorenzelli, FT-IR study of the adsorption and transformation of formaldehyde on oxide surfaces. *J. Am. Chem. Soc.* **109**, 5197-5202 (1987).
2. C.-H. Huang, M. Tang, C. Shi, P. A. Iglesias, P. N. Devreotes, An excitable signal integrator couples to an idling cytoskeletal oscillator to drive cell migration. *Nat. Cell Biol.* **15**, 1307-1316 (2013).
3. V. M. Ortega-Jimenez, R. Dudley, Aerial shaking performance of wet Anna's hummingbirds. *J. Royal Soc. Interface* **9**, 1093-1099 (2012).
4. K. Kruse, F. Jülicher, Oscillations in cell biology. *Curr. Opin. Cell Biol.* **17**, 20-26 (2005).
5. H. Zeng, M. Lahikainen, L. Liu, Z. Ahmed, O. M. Wani, M. Wang, H. Yang, A. Priimagi, Light-fuelled freestyle self-oscillators. *Nat. Commun.* **10**, 1-9 (2019).
6. P. Lenz, L. Søgaard-Andersen, Temporal and spatial oscillations in bacteria. *Nat. Rev. Microbiol.* **9**, 565-577 (2011).
7. T. Y.-C. Tsai, Y. S. Choi, W. Ma, J. R. Pomerening, C. Tang, J. E. Ferrell, Robust, tunable biological oscillations from interlinked positive and negative feedback loops. *Science* **321**, 126-129 (2008).
8. H. Cui, Q. Zhao, Y. Wang, X. Du, Bioinspired Actuators Based on Stimuli-Responsive Polymers. *Chem. Asian J.* **14**, 2369-2387 (2019).
9. S. Maeda, Y. Hara, T. Sakai, R. Yoshida, S. Hashimoto, Self-walking gel. *Adv. Mater.* **19**, 3480-3484 (2007).
10. Y. Wu, J. K. Yim, J. Liang, Z. Shao, M. Qi, J. Zhong, Z. Luo, X. Yan, M. Zhang, X. Wang, Insect-scale fast moving and ultrarobust soft robot. *Sci. Robot.* **4**, eaax1594 (2019).
11. T. Li, G. Li, Y. Liang, T. Cheng, J. Dai, X. Yang, B. Liu, Z. Zeng, Z. Huang, Y. Luo, Fast-moving soft electronic fish. *Sci. Adv.* **3**, e1602045 (2017).
12. G. Gu, J. Zou, R. Zhao, X. Zhao, X. Zhu, Soft wall-climbing robots. *Sci. Robot.* **3**, eaat2874 (2018).
13. P. Rothemund, A. Ainla, L. Belding, D. J. Preston, S. Kurihara, Z. Suo, G. M. Whitesides, A soft, bistable valve for autonomous control of soft actuators. *Sci. Robot.* **3**, eaar7986 (2018).
14. A. Rafsanjani, Y. Zhang, B. Liu, S. M. Rubinstein, K. Bertoldi, Kirigami skins make a simple soft actuator crawl. *Sci. Robot.* **3**, eaar7555 (2018).
15. D. W. Haldane, M. M. Plecnik, J. K. Yim, R. S. Fearing, Robotic vertical jumping agility via series-elastic power modulation. *Sci. Robot.* **1**, eaag2048 (2016).
16. Y. Kim, H. Yuk, R. Zhao, S. A. Chester, X. Zhao, Printing ferromagnetic domains for untethered fast-transforming soft materials. *Nature* **558**, 274-279 (2018).
17. Z. Li, Y. Yin, Stimuli-responsive optical nanomaterials. *Adv. Mater.* **31**, 1807061 (2019).
18. M. Hua, C. Kim, Y. Du, D. Wu, R. Bai, X. He, Swaying gel: chemo-mechanical self-oscillation based on dynamic buckling. *Matter* **4**, 1029-1041 (2021).
19. X.-Q. Wang, C. F. Tan, K. H. Chan, X. Lu, L. Zhu, S.-W. Kim, G. W. Ho, In-built thermo-mechanical cooperative feedback mechanism for self-propelled multimodal locomotion and electricity generation. *Nat. Commun.* **9**, 1-10 (2018).
20. Y. S. Kim, M. Liu, Y. Ishida, Y. Ebina, M. Osada, T. Sasaki, T. Hikima, M. Takata, T. Aida, Thermoresponsive actuation enabled by permittivity switching in an electrostatically anisotropic hydrogel. *Nature Mater.* **14**, 1002-1007 (2015).
21. R. Yoshida, T. Ueki, Evolution of self-oscillating polymer gels as autonomous polymer systems. *NPG Asia Mater.* **6**, e107-e107 (2014).
22. H. Arazoe, D. Miyajima, K. Akaike, F. Araoka, E. Sato, T. Hikima, M. Kawamoto, T. Aida, An autonomous actuator driven by fluctuations in ambient humidity. *Nature Mater.* **15**, 1084-1089 (2016).

23. B. Shin, J. Ha, M. Lee, K. Park, G. H. Park, T. H. Choi, K.-J. Cho, H.-Y. Kim, Hygrobot: A self-locomotive ratcheted actuator powered by environmental humidity. *Sci. Robot.* **3**, eaar2629 (2018).
24. Z. Li, Y. Yin, Creating chameleon-like smart actuators. *Matter* **1**, 550-551 (2019).
25. Y. Wang, H. Cui, Q. Zhao, X. Du, Chameleon-inspired structural-color actuators. *Matter* **1**, 626-638 (2019).
26. X. Lu, H. Zhang, G. Fei, B. Yu, X. Tong, H. Xia, Y. Zhao, Liquid‐crystalline dynamic networks doped with gold nanorods showing enhanced photocontrol of actuation. *Adv. Mater.* **30**, 1706597 (2018).
27. X. Qian, Y. Zhao, Y. Alsaid, X. Wang, M. Hua, T. Galy, H. Gopalakrishna, Y. Yang, J. Cui, N. Liu, Artificial phototropism for omnidirectional tracking and harvesting of light. *Nat. Nanotechnol.* **14**, 1048-1055 (2019).
28. Z. Sun, Y. Yamauchi, F. Araoka, Y. S. Kim, J. Bergueiro, Y. Ishida, Y. Ebina, T. Sasaki, T. Hikima, T. Aida, An Anisotropic Hydrogel Actuator Enabling Earthworm-Like Directed Peristaltic Crawling. *Angew. Chem. Int. Ed.* **57**, 15772-15776 (2018).
29. Z. Li, Z. Ye, L. Han, Q. Fan, C. Wu, D. Ding, H. L. Xin, N. V. Myung, Y. Yin, Polarization-modulated multidirectional photothermal actuators. *Adv. Mater.* **33**, 2006367 (2021).
30. Y. Zhao, C.-Y. Lo, L. Ruan, C.-H. Pi, C. Kim, Y. Alsaid, I. Frenkel, R. Rico, T.-C. Tsao, X. He, Somatosensory actuator based on stretchable conductive photothermally responsive hydrogel. *Sci. Robot.* **6**, eabd5483 (2021).
31. A. H. Gelebart, G. Vantomme, E. Meijer, D. J. Broer, Mastering the photothermal effect in liquid crystal networks: a general approach for self-sustained mechanical oscillators. *Adv. Mater.* **29**, 1606712 (2017).
32. A. H. Gelebart, D. J. Mulder, M. Varga, A. Konya, G. Vantomme, E. Meijer, R. L. Selinger, D. J. Broer, Making waves in a photoactive polymer film. *Nature* **546**, 632-636 (2017).
33. K. Kumar, C. Knie, D. Bléger, M. A. Peletier, H. Friedrich, S. Hecht, D. J. Broer, M. G. Debije, A. P. Schenning, A chaotic self-oscillating sunlight-driven polymer actuator. *Nat. Commun.* **7**, 1-8 (2016).
34. X. Qian, Y. Zhao, Y. Alsaid, X. Wang, M. Hua, T. Galy, H. Gopalakrishna, Y. Yang, J. Cui, N. Liu, Artificial phototropism for omnidirectional tracking and harvesting of light. *Nat. Nanotechnol* **14**, 1048-1055 (2019).
35. Y. Zhao, C. Xuan, X. Qian, Y. Alsaid, M. Hua, L. Jin, X. He, Soft phototactic swimmer based on self-sustained hydrogel oscillator. *Sci. Robot.* **4**, eaax7112 (2019).
36. J. Chen, J. Feng, F. Yang, R. Aleisa, Q. Zhang, Y. Yin, Space-Confined Seeded Growth of Cu Nanorods with Strong Surface Plasmon Resonance for Photothermal Actuation. *Angew. Chem. Int. Ed.* **58**, 9275-9281 (2019).
37. Z. Li, Q. Fan, C. Wu, Y. Li, C. Cheng, Y. Yin, Magnetically Tunable Plasmon Coupling of Au Nanoshells Enabled by Space-Free Confined Growth. *Nano Lett.* **20**, 8242-8249 (2020).
38. Z. Li, J. Jin, F. Yang, N. Song, Y. Yin, Coupling magnetic and plasmonic anisotropy in hybrid nanorods for mechanochromic responses. *Nat. Commun.* **11**, 1-11 (2020).
39. W. Xu, M. Wang, Z. Li, X. Wang, Y. Wang, M. Xing, Y. Yin, Chemical transformation of colloidal nanostructures with morphological preservation by surface-protection with capping ligands. *Nano Lett.* **17**, 2713-2718 (2017).
40. D. Armani, C. Liu, N. Aluru, in *Technical Digest. IEEE International MEMS 99 Conference. Twelfth IEEE International Conference on Micro Electro Mechanical Systems (Cat. No. 99CH36291)*. (IEEE, 1999), pp. 222-227.
41. Y. Bai, B. Chen, F. Xiang, J. Zhou, H. Wang, Z. Suo, Transparent hydrogel with enhanced water retention capacity by introducing highly hydratable salt. *Appl. Phys. Lett.* **105**, 151903 (2014).
42. X. Zhou, Y. Guo, F. Zhao, G. Yu, Hydrogels as an emerging material platform for solar water purification. *Acc. Chem. Res.* **52**, 3244-3253 (2019).

43. Y. Sekine, T. Ikeda-Fukazawa, Structural changes of water in a hydrogel during dehydration. *J. Chem. Phys.* **130**, 034501 (2009).
44. S. H. Shaikh, S. A. Kumar, Polyhydroxamic acid functionalized sorbent for effective removal of chromium from ground water and chromic acid cleaning bath. *Chem. Eng. J.* **326**, 318-328 (2017).
45. Y. Zaitsev, P. Liss, Neuston of seas and oceans. *The sea surface and global change*, 371-382 (2005).
46. Y. S. Song, M. Sitti, Surface-tension-driven biologically inspired water strider robots: Theory and experiments. *IEEE Trans. Robot.* **23**, 578-589 (2007).
47. X.-Q. Feng, X. Gao, Z. Wu, L. Jiang, Q.-S. Zheng, Superior water repellency of water strider legs with hierarchical structures: experiments and analysis. *Langmuir* **23**, 4892-4896 (2007).
48. Z. Li, Y. Liu, M. Marin, Y. Yin, Thickness-dependent wrinkling of PDMS films for programmable mechanochromic responses. *Nano Res.* **13**, 1882-1888 (2020).
49. J. Iriarte-Díaz, Differential scaling of locomotor performance in small and large terrestrial mammals. *J. Exp. Biol.* **205**, 2897-2908 (2002).
50. J. Blaxter, W. Dickson, Observations on the swimming speeds of fish. *ICES J. Mar. Sci.* **24**, 472-479 (1959).
51. R. Bainbridge, The speed of swimming of fish as related to size and to the frequency and amplitude of the tail beat. *J. Exp. Biol.* **35**, 109-133 (1958).
52. D. L. Hu, B. Chan, J. W. Bush, The hydrodynamics of water strider locomotion. *Nature* **424**, 663-666 (2003).

Acknowledgments: We thank the financial support from the U.S. National Science Foundation. N. V. M. and Y. Y. are members of the UC-KIMS Center for Innovation Materials for Energy and Environment jointly supported by UC Riverside and Korea Institute of Materials Science. **Funding:** Supported by the U.S. National Science Foundation (CHE-1808788). **Author contributions**: Z. L., N. V. M., and Y. Y. conceived the concept and designed the research plans. N. V. M. and Y. Y. supervised the research. Z. L. performed the experiments and developed the analytic model. Z. L. wrote the manuscript and N. V. M., and Y. Y. revised the manuscript. **Competing interests**: All authors declare they have no competing interests. **Data and materials availability**: All data needed to evaluate the conclusions in the paper are present in the paper or the Supplementary Materials.

Fig. 1. Photothermal oscillators powered by local steam generation. (A) Schematic illustration of the trilayer structure of the actuators. (B) Working mechanism of the hydrogel oscillation driven by photothermal steam generation. Digital photos showing the (C) bending and (D) oscillation of the actuators under NIR light irradiation. (E) Time-resolved bending angles during oscillation. (F) Corresponding fast Fourier transform (FFT) of the bending angles.

Fig. 2. Tuning the oscillation frequency by controlling film geometry. (A) Oscillation amplitude of films with different lengths. (B) FFT of film oscillation for different lengths. (C) Dependence of oscillation frequency on film length. Error bars indicate standard deviation (SD) based on three measurements. (D) Dependence of maximum bending and relaxing velocity of the trilayer oscillators on the film thickness. (E) The oscillation frequency as a function of film thickness.

Fig. 3. Tuning oscillation frequency by controlling the hydrogel crosslinking ratio. (A) Digital pictures and (B) schemes of the hydrogel films with different crosslinking ratios. Scale bar in (A): 0.5 cm. (C) The hydration performance of the hydrogel films with different crosslinking ratios. (D) Dependence of water content on hydrogel crosslinking ratios. (E) Dependence of oscillation frequency and magnitude of the hydrogel oscillators on crosslinking ratios. Error bars indicate SD based on three measurements.

Fig. 4. Pulsed and damped harmonic photothermal oscillation. (A) Hydrogel oscillation under NIR light irradiation with different input energy. (B) FFT of the hydrogel oscillation. Inset defines the oscillation periodicity (t_1) and pulse periodicity (t_2). (C) Dependence of the oscillation (f_1) and pulse frequency (f_2) on light intensity. (D) Digital pictures of the steam bubble evolution and (E) the coherent film bending under NIR light irradiation. Scale bars in (D) and (E): 2 mm. (F) Time-resolved steam bubble size and (G) film bending angles. The (i), (ii), (iii), (iv), and (v) in Figs. 4D-4G represent the initial equilibrium state, state with maximum bubble size, and states under the first, second, and third oscillation peaks of the middle pulse in Fig. 4G, respectively. The values in Fig. 4F represent corresponding bubble diameters in millimeters in the five states.

Fig. 5. A biomimetic photothermal NeusBot. Digital pictures of (A) the curved trilayer film and (B) hydrogel swimmer at the air-water interface. (C) Scheme of the hydrogel oscillator swimming at the air-water interface. (D) Path length, (E) real-time positions, and (F) velocity of the swimmer while shining constant light with different input powers. In (F), the light intensity for panels from bottom to top is 0.2 W to 0.4 W, 0.6 W, 0.8 W, and 1.2 W, respectively, with a beam diameter of 3.8 mm. (G) Summary of the swimming performances of natural creatures and artificial soft swimmers.

Fig. 6. Controlling the direction of the photothermal swimmer. (A) Scheme (i) and the real-time x-y coordinates (ii) of the hydrogel swimmer in clockwise turning. (B) Scheme (i) and the real-time x-y coordinates (ii) during counterclockwise turning. Time-resolved displacement in (C) clockwise and (D) counterclockwise turning. (E) Real-time rotation angles of the hydrogel swimmers. (F) Polar plot showing the direction of the swimmers under NIR light irradiation for arbitrary durations. The radius represents time in seconds.

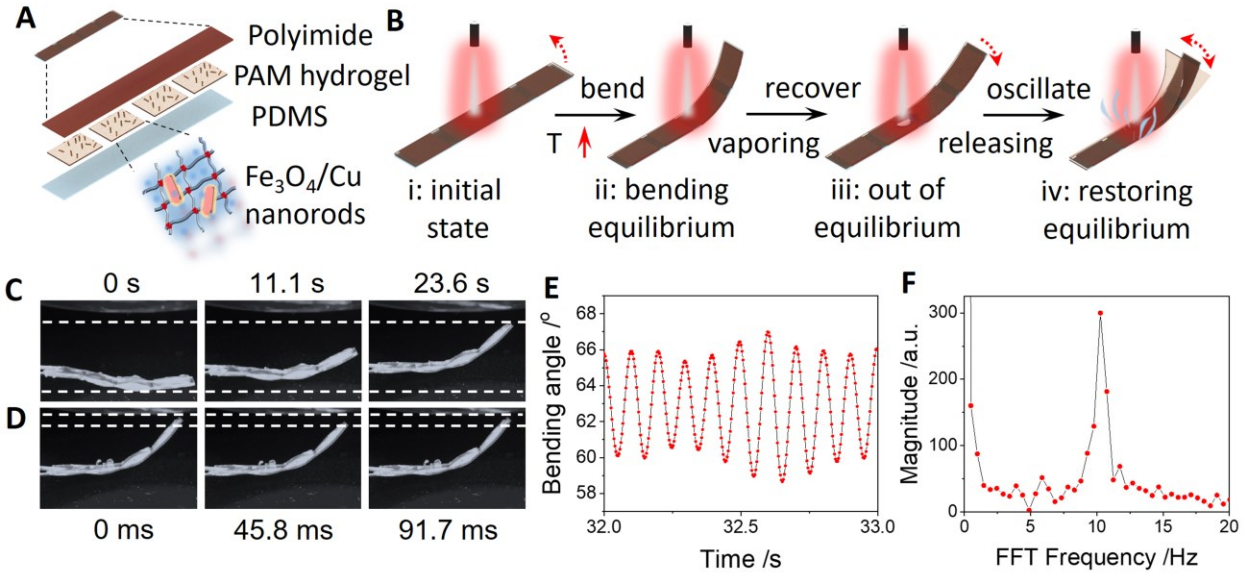
A
Polyimide
PAM hydrogel
PDMS
Fe_3O_4/Cu
nanorods
B
bend
recover
oscillate
T
vaporing
releasing
i: initial
state
ii: bending
equilibrium
iii: out of
equilibrium
iv: restoring
equilibrium
C
0 s
11.1 s
23.6 s
D
0 ms
45.8 ms
91.7 ms
E
Bending angle /°
68
66
64
62
60
58
32.0
32.5
33.0
Time /s
F
Magnitude /a.u.
300
200
100
0
0
5
10
15
20
FFT Frequency /Hz

Figure 1

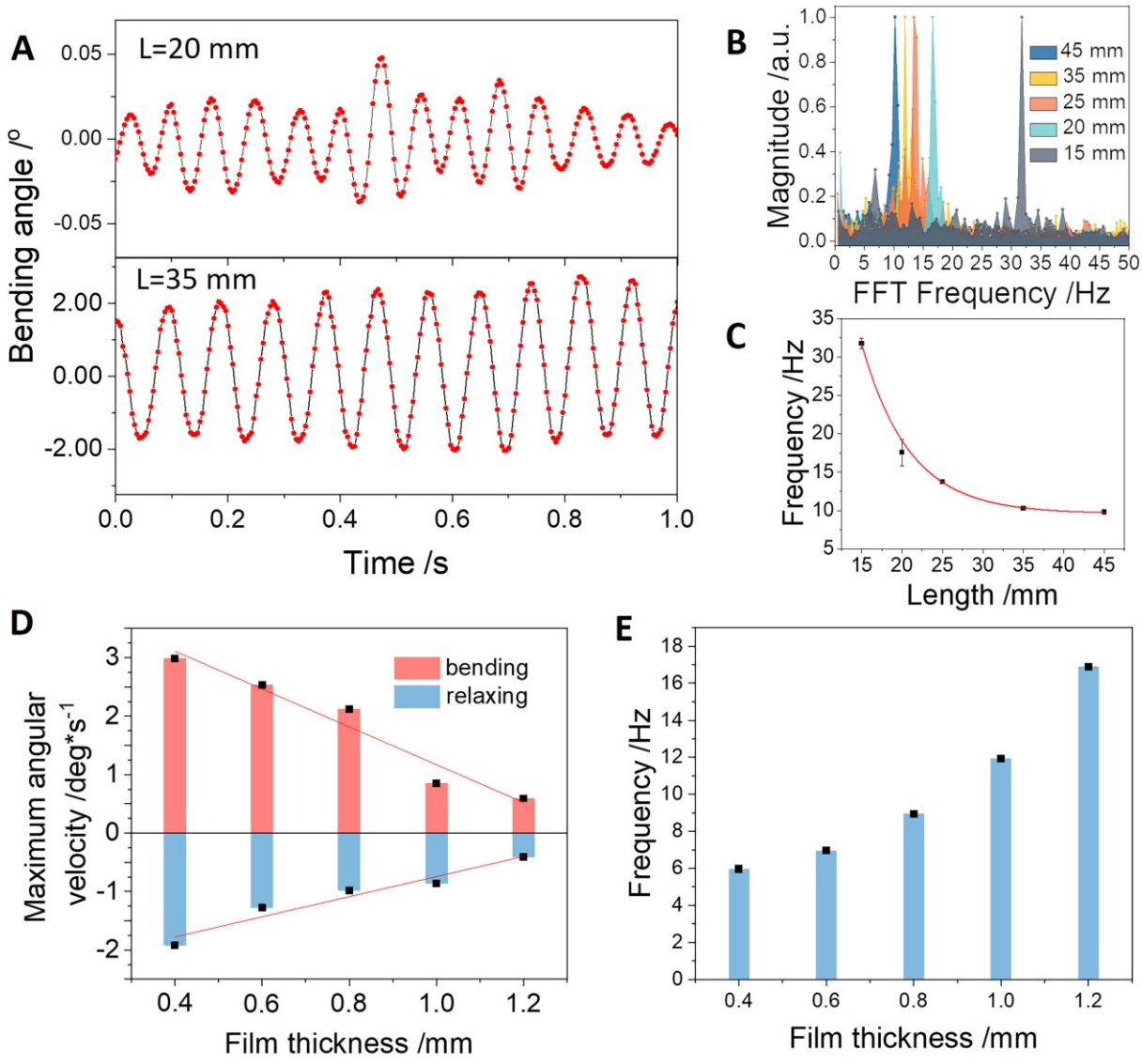
A
L=20 mm
L=35 mm
Bending angle /°
Time /s
B
Magnitude /a.u.
FFT Frequency /Hz
45 mm
35 mm
25 mm
20 mm
15 mm
C
Frequency /Hz
Length /mm
D
Maximum angular velocity /deg*s-1
bending
relaxing
Film thickness /mm
E
Frequency /Hz
Film thickness /mm

Figure 2

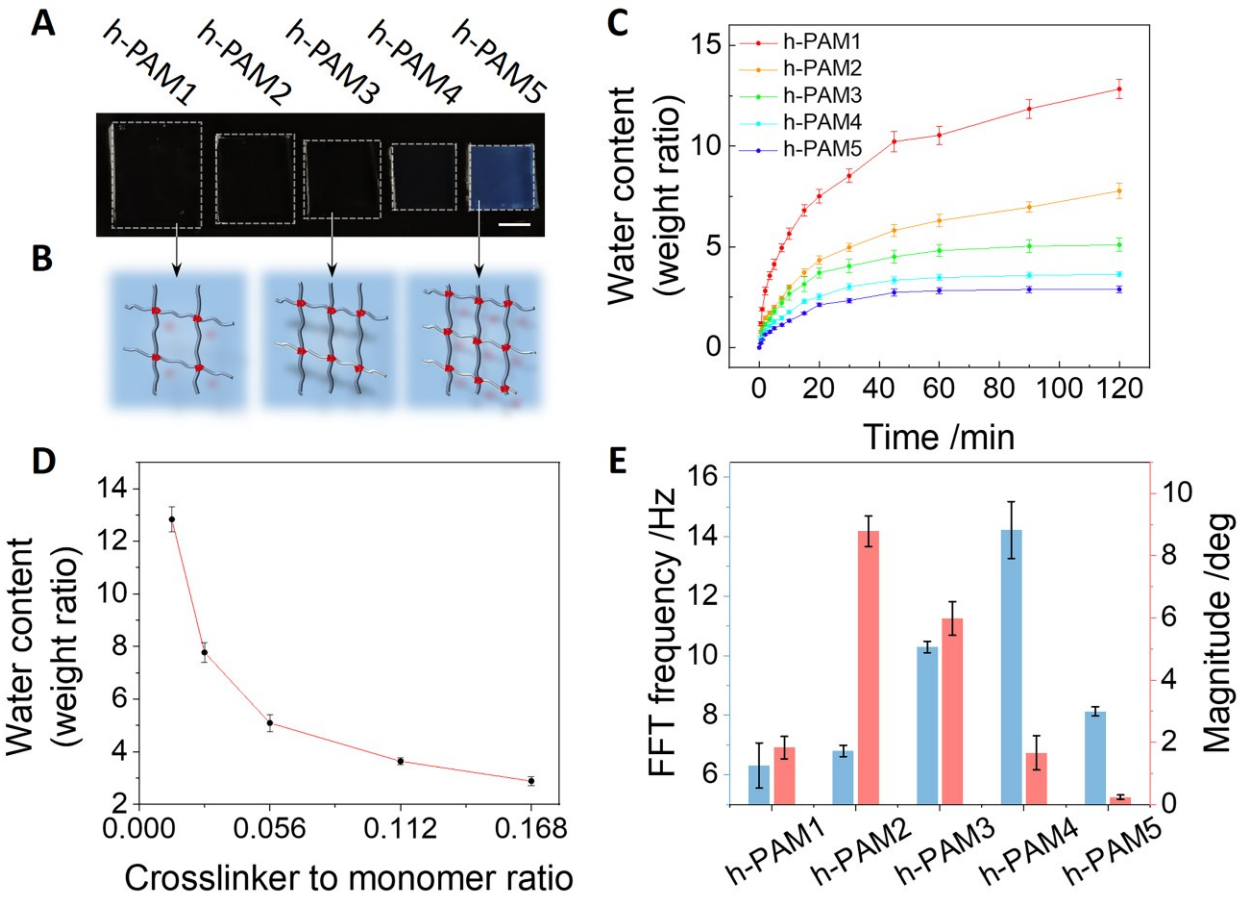
A
h-PAM1
h-PAM2
h-PAM3
h-PAM4
h-PAM5
B
C
Water content (weight ratio)
Time /min
D
Water content (weight ratio)
Crosslinker to monomer ratio
E
FFT frequency /Hz
Magnitude /deg

Figure 3

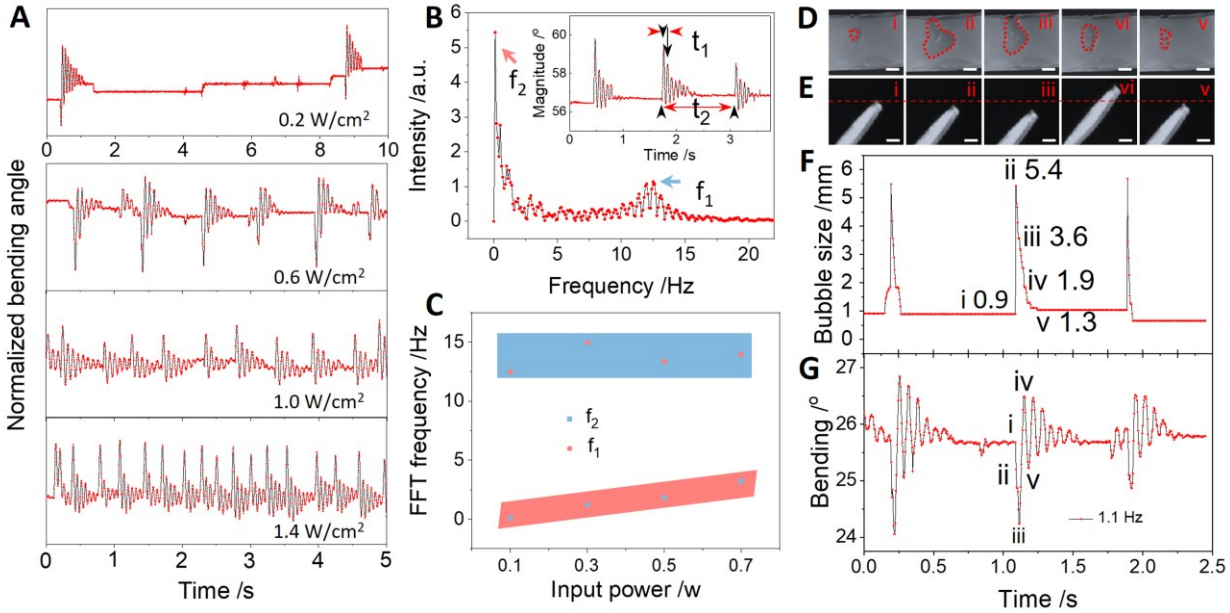
A
0.2 W/cm²
0.6 W/cm²
1.0 W/cm²
1.4 W/cm²
Normalized bending angle
Time /s
B
Intensity /a.u.
Frequency /Hz
f2
f1
t1
t2
Magnitude /°
Time /s
C
FFT frequency /Hz
Input power /w
f2
f1
D
E
F
Bubble size /mm
i 0.9
ii 5.4
iii 3.6
iv 1.9
v 1.3
G
Bending /°
1.1 Hz
Time /s

Figure 4

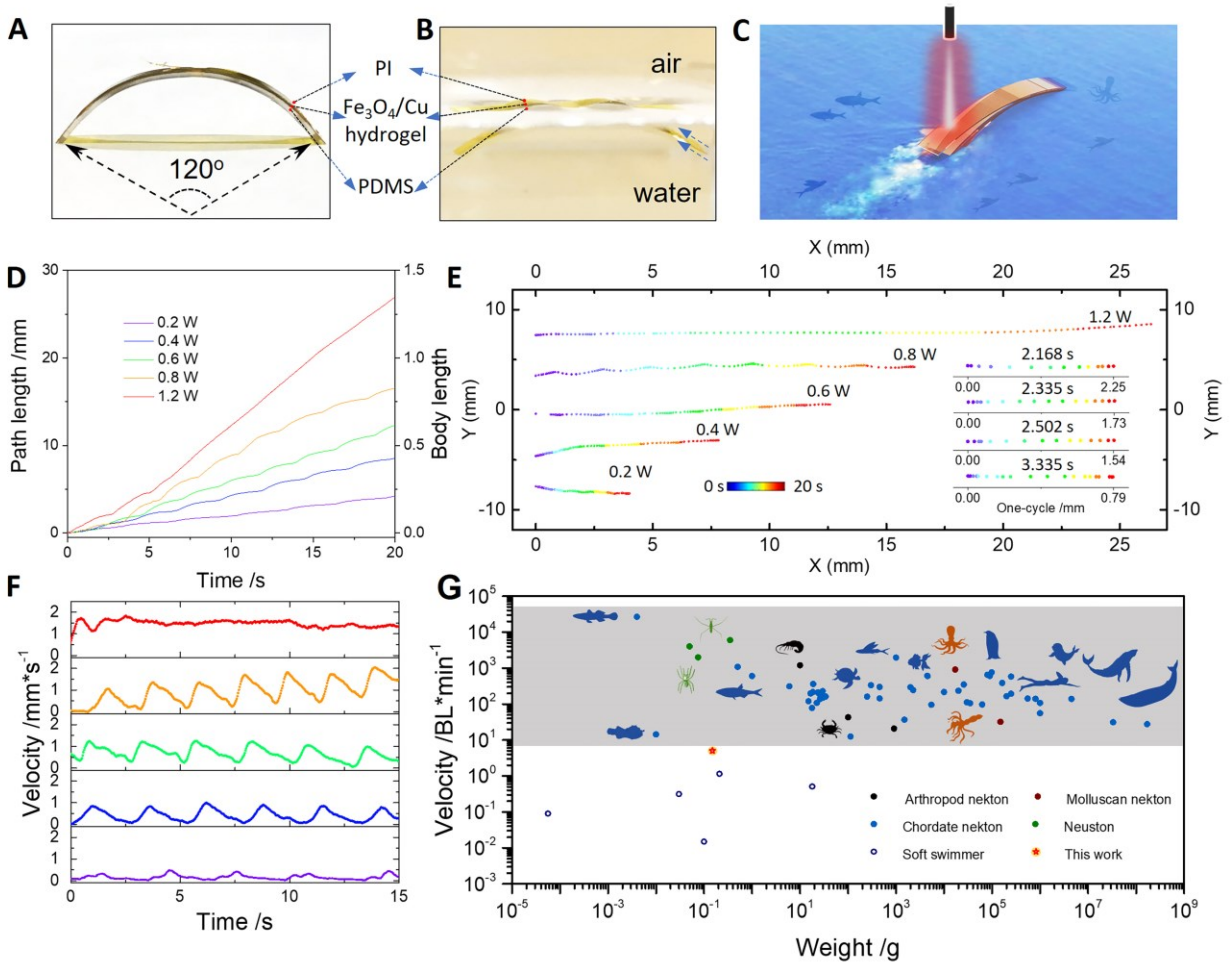
A
120°
PI
Fe3O4/Cu
hydrogel
PDMS
B
air
water
C
D
Path length /mm
Body length
Time /s
0.2 W
0.4 W
0.6 W
0.8 W
1.2 W
E
X (mm)
Y (mm)
1.2 W
0.8 W
0.6 W
0.4 W
0.2 W
0 s
20 s
2.168 s
2.335 s
2.502 s
3.335 s
One-cycle /mm
F
Velocity /mm*s-1
Time /s
G
Velocity /BL*min-1
Weight /g
Arthropod nekton
Molluscan nekton
Chordate nekton
Neuston
Soft swimmer
This work

Figure 5

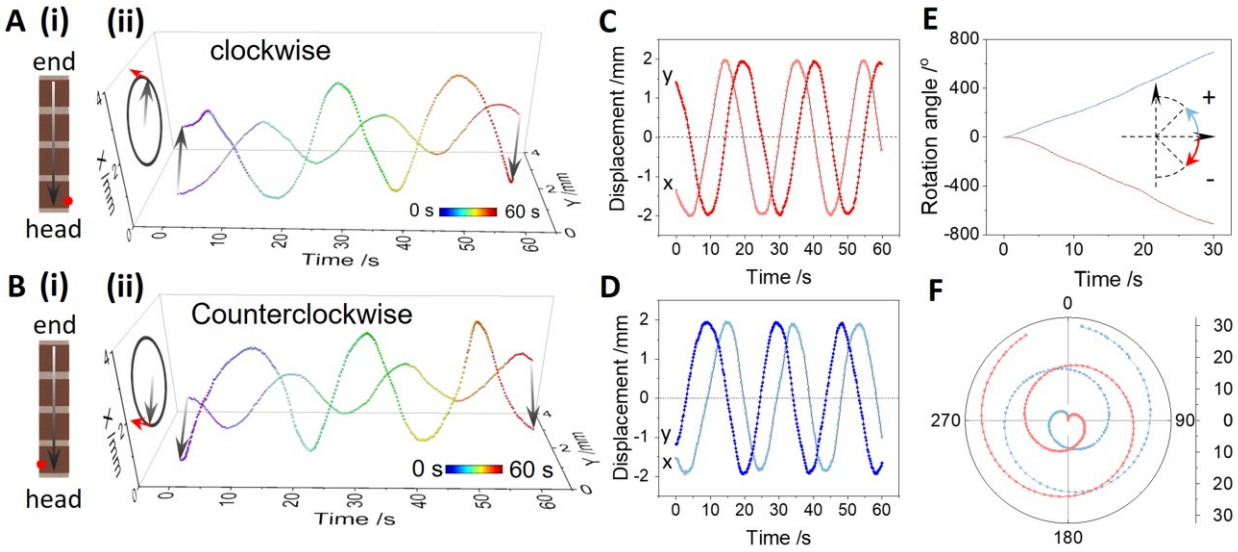
A (i)
(ii)
end
head
clockwise
0 s
60 s
Time /s
B (i)
(ii)
end
head
Counterclockwise
0 s
60 s
Time /s
C
Displacement /mm
y
x
Time /s
D
Displacement /mm
y
x
Time /s
E
Rotation angle /°
+
-
Time /s
F
0
90
180
270

Figure 6